

This paper has been accepted for publication in Applied Surface Science. DOI: <https://doi.org/10.1016/j.apsusc.2023.157476>

Direct atomic layer deposition of ultra-thin Al₂O₃ and HfO₂ films on gold-supported monolayer MoS₂

E. Schilirò^{1*}, S. E. Panasci¹, A.M. Mio¹, G. Nicotra¹, S. Agnello^{2,1,3}, B. Pecz⁴, G.Z. Radnoczi⁴, I. Deretzis¹, A. La Magna¹, F. Roccaforte¹, R. Lo Nigro¹, F. Giannazzo¹

¹ CNR-IMM, Strada VIII, 5 95121, Catania, Italy

² Department of Physics and Chemistry, University of Palermo, Via Archirafi 36, 90143 Palermo, Italy

³ ATeN Center, Viale delle Scienze Ed. 18, 90128 Palermo, Italy

⁴ Institute for Technical Physics and Materials Science, Centre for Energy Research, HAS, 1121 Konkoly-Thege 29-33, Budapest, Hungary

*e-mail: emanuela.schiliro@imm.cnr.it

Abstract

In this paper, the atomic layer deposition (ALD) of ultra-thin films (<4 nm) of Al₂O₃ and HfO₂ on gold-supported monolayer (1L) MoS₂ is investigated, providing an insight on the mechanisms ruling the nucleation in the early stages of the ALD process. A preliminary multiscale characterization of large area 1L-MoS₂ exfoliated on sputter-grown Au/Ni films demonstrated: (i) a tensile strain (from 0.1 to 0.3%) and p-type doping (from 1×10^{12} to 4×10^{12} cm⁻²) distribution at micro-scale; (ii) an almost conformal MoS₂ membrane to the Au grains topography, with some locally detached regions, indicating the occurrence of strain variations at the nanoscale; (iii) atomic scale variability (from ~4.0 to ~4.5 Å) in the Mo-Au atomic distances was detected, depending on the local configuration of Au nanograins. *Ab initio* DFT calculations of a free-standing MoS₂ layer and a simplified MoS₂/Au(111) interface model showed a significant influence of the Au substrate on the MoS₂ energy band structure, whereas small differences were accounted for the adsorption of H₂O, TMA (co-reactant, and Al-precursor, respectively) molecules, and a slight improved adsorption was predicted for TDMAHf

(Hf-precursor). This suggests a crucial role of nanoscale morphological effects, such as the experimentally observed local curvature and strain of the MoS₂ membrane, in the enhanced physisorption of the precursors. Afterwards the nucleation and growth of Al₂O₃ and HfO₂ films onto 1L-MoS₂/Au was investigated in detail, by monitoring the surface coverage as a function of the number (N) of ALD cycles, with N from 10 to 120. At low N values, a slower growth rate of the initially formed nuclei was observed for HfO₂, probably due to the bulky nature of the TDMAHf precursor as compared to TMA. On the other hand, the formation of continuous films was obtained in both cases for N>80 ALD cycles, corresponding to ~3.6 nm Al₂O₃ and ~3.1 nm HfO₂. Current mapping on these ultra-thin films by conductive-AFM showed, for the same applied bias, a uniform insulating behavior of Al₂O₃ and the occurrence of few localized breakdown spots in the case of HfO₂, associated to a less compact films regions. Finally, an increase of the 1L-MoS₂ tensile strain was observed by Raman mapping after encapsulation with both high-κ films, accompanied by a reduction in the PL intensity, explained by the effects of strain and the higher effective dielectric constant of the surrounding environment.

1. Introduction

Molybdenum disulfide (2H-MoS₂) is currently the most investigated two dimensional (2D) material in the transition metal dichalcogenides (TMDs) class. Due to its peculiar tunable semiconducting behavior, characterized by a direct band-gap of 1.8 eV for monolayer (1L) and an indirect band-gap of 1.2 eV for few layers and bulk films[1,2], it is very promising for logic and switching electronic devices. In this respect, the integration of high-κ dielectrics, such as Al₂O₃ and HfO₂, on MoS₂ surface proved to be essential for obtaining high performance in terms of field-effect mobility (100-500 cm²/V s), sub-threshold swing (~ 70 mV/dec), and on/off ratio (~ 10⁸) in MoS₂-based field effect transistors [3,4,5]. Currently, the atomic layer deposition (ALD) represents the technique of choice for the growth of high-κ dielectrics in microelectronics, thanks to its peculiar working principle (consisting of a series of self-limited reaction cycles between precursors) that guarantees a nanometric thickness control, conformity, and uniformity on large areas [6]. However, the direct ALD on MoS₂ and other 2D materials, is typically hindered by the lack of out-of-plane bonds on the surface of van der Waals materials, which should act as nucleation sites for ALD precursors [7,8]. To circumvent this issue, different approaches have been explored to enhance the ALD growth on the 2D-materials, including the pre-deposition of seed-layers and pre-functionalization processes are the most used methods [9,10,11,12]. Actually, such approaches allow to achieve a uniform high-k dielectrics

coverage on the MoS₂ surface. On the other hand, they affect the interface quality and ultimately limit the minimum deposited dielectric thickness. Besides using seed-layers and pre-functionalization treatments, the ALD process on the 2D materials can be also improved by adjusting the deposition parameters, including temperature, reactivity of co-reactants (H₂O, O₂-plasma, O₃) and precursor flow [13, 15]. The temperature of the ALD process has been found to be determinant for the uniformity of growth on MoS₂. In particular, temperatures lower than 150°C improve the Al₂O₃ coverage, by limiting the desorption phenomena of the ALD-precursor, i.e. trimethylaluminium (TMA) [8]. On the other hand, low deposition temperatures result in a poor structural and electrical quality of the dielectric, as a consequence of a decreased reactivity of ALD precursors [14]. Also resorting to more reactive ALD co-reactants, such as O₃ instead of H₂O [15], or using O₂-plasma pre-treatments of the MoS₂ surface [16], can be useful to optimize the uniformity of dielectrics on MoS₂. Unfortunately, such treatments can be detrimental for MoS₂ due to defects and MoO₃ formation. For these reasons, optimizing a direct thermal ALD process, without the above-mentioned seed-layers and pre-functionalization approaches, can be essential to achieve ultra-thin dielectric films on MoS₂, while preserving its structural integrity.

In the last years, different authors reported on the enhanced ALD nucleation of high-k dielectrics on monolayers (1L) of 2D materials, promoted by the interaction with the underlying substrate [17]. Such a behavior was first observed during thermal ALD of Al₂O₃ on CVD-grown graphene on copper [18], where the activation of the ALD process was attributed to peculiar polar sites produced by the graphene/metal interaction, acting as traps for the adsorption of the ALD-precursor [19,20]. An enhanced nucleation has been reported also in the early stages of thermal ALD of Al₂O₃ on top of 1L epitaxial graphene on 4H-SiC(0001), and it was ascribed to the peculiar interface structure of graphene with the SiC substrate [21,22]. This is characterized by the presence of an sp³ carbon buffer layer, partially covalently bonded to the underlying Si face of SiC with a large density of positively charged dangling bonds, which are responsible of high n-type doping of epitaxial graphene. Ab-initio DFT calculations predicted an enhanced adsorption of the H₂O polar molecules, the co-reactants in the ALD process, on the highly doped graphene surface [22]. Furthermore, the compressive strain of epitaxial graphene on SiC was expected to significantly contribute to the increased reactivity with respect to an ideal free-standing graphene [22].

More recently, the direct growth of very uniform and ultra-thin (~4 nm) Al₂O₃ films with very good insulating properties has been achieved by thermal ALD at 250 °C upon 1L-MoS₂ membranes exfoliated on a gold substrate [17]. Interestingly, using identical ALD deposition conditions, an inhomogeneous Al₂O₃ coverage was observed for 1L-MoS₂ membranes produced by gold-assisted exfoliation and transferred onto an insulating Al₂O₃/Si substrate. The enhanced Al₂O₃ nucleation on

the Au-supported 1L-MoS₂ was ascribed to an increased reactivity of MoS₂, originating from the strong S-Au interaction at MoS₂/gold interface [23,24]. However, the exact nanoscale mechanisms ruling the improved physisorption/chemisorption of the precursors and/or co-reactant molecules on the 1L-MoS₂/Au system during the early stages of the ALD process need to be further investigated, in view of future applications of this approach. Furthermore, it would be useful to understand whether the observed behavior is limited to the Al₂O₃ precursors or it can be extended to the ALD deposition of other high-k insulators, such as HfO₂, which are interesting for MoS₂ applications in electronics [25,26,27]. The commonly used Al precursor in the ALD growth of Al₂O₃, i.e. trimethylaluminum (TMA, Al(CH₃)₃) [28], is a relatively small molecule. On the other hand, the most frequently used Hf precursor for HfO₂ ALD growth, i.e. the tetrakis-dimethylaminohafnium (TDMAHf), exhibits a bulky structure, which can influence the nucleation degree due to steric hindrance [29].

In this paper, an insight on the possible mechanisms responsible of the enhanced reactivity of Au-supported 1L-MoS₂ towards the species involved in the thermal ALD process has been provided. The nanoscale structural/morphological properties and doping/strain for the experimental 1L-MoS₂/Au system has been initially assessed, and complemented by the predictions from ab-initio density functional theory (DFT) calculations for an ideal MoS₂/Au(111) heterojunction. Furthermore, the nucleation and growth of ultra-thin films of Al₂O₃ and HfO₂ on the surface of Au-supported 1L-MoS₂ under optimized ALD conditions was comparatively investigated by detailed atomic force microscopy investigations. By systematically following the surface coverage as a function of the number (N) of ALD cycles (N from 10 to 120), significant differences were observed between Al₂O₃ and HfO₂ (especially at lower N), and ascribed to the different nature of the used precursors. Finally, the insulating quality of uniform Al₂O₃ and HfO₂ films, obtained after 80 ALD cycles on 1L-MoS₂/Au, were assessed by nanoscale current mapping using conductive atomic force microscopy (CAFM), whereas their impact on the vibrational and light emission properties of MoS₂ has been investigated by Raman and Photoluminescence (PL) spectra.

2. Materials and Methods

The substrate material used in these experiments consisted of ~8 nm Ni wetting layer and ~10 nm Au film, sequentially deposited on a SiO₂/Si sample by DC magnetron sputtering. Therefore, a bulk molybdenite stamp was pressed on the freshly prepared Au surface, resulting in the effective exfoliation of ultra-thin and extended (cm²) MoS₂ membranes, mostly formed by 1L-MoS₂ [23, 30,31,32,33,34,35,36].

Thermal ALD of Al₂O₃ and HfO₂ on the surface of the 1L-MoS₂/Au system was performed using in both cases H₂O as the co-reactant, while trimethylaluminum (TMA) and

tetrakisdimethylaminohafnium (TDMAH) $\text{Hf} [\text{N}(\text{CH}_3)_2]_4$ were used as precursors for Al_2O_3 and HfO_2 , respectively. During the Al_2O_3 process, the precursors pulse times of 20 ms were used for TMA and H_2O . Differently, for the HfO_2 , the precursor pulse times were 40 ms and 20 ms for TDMAHf and H_2O , respectively. After each pulse, a purging N_2 was introduced in the chamber to remove unreacted precursors. The deposition temperatures, opportunely optimized for the two different precursors, were 250°C and 290°C for Al_2O_3 and HfO_2 , respectively [37]. The pressure in the chamber during both processes was 10 Pa. The growth mechanism of the two high- κ dielectrics has been investigated on a set of consecutive ALD processes, increasing the number of deposition cycles, from 10 to 40, 80 and 120. The number of deposition cycles have been chosen identical for both dielectrics, considering the same growth rate of $0.88 \text{ \AA}/\text{cycle}$ calibrated on a silicon substrate.

The structural properties of the MoS_2 membranes exfoliated on the $\text{Au}/\text{Ni}/\text{SiO}_2$ substrate have been investigated with atomic resolution by electron microscopy on cross-sectioned lamellas, prepared by focused-ion-beam (FIB). First, high-resolution transmission electron microscopy (HRTEM), scanning transmission electron microscopy (STEM) in high-angle-annular-dark-field (HAADF) mode, and energy dispersive spectroscopy (EDS) analyses were acquired using an image corrected ThermoFisher THEMIS 200 microscope with 200 keV electron beam. Furthermore, atomic resolution analyses of the MoS_2/Au interface by STEM in the HAADF mode have been performed at primary electron beam energy of 200 keV using a probe corrected JEOL ARM 200F microscope.

The morphology of the as-exfoliated 1L- MoS_2 on gold, and the coverage degree of Al_2O_3 and HfO_2 on MoS_2 after different ALD cycles have been examined by tapping mode Atomic Force Microscopy (AFM), using a DI3100 equipment by Bruker with Nanoscope V electronics. Sharp silicon tips with a curvature radius of $\sim 5 \text{ nm}$ were used for these measurements. The insulating properties of the high- κ films onto MoS_2/Au have been also evaluated by conductive-AFM (C-AFM) using the TUNA module by Bruker and Pt-coated Si tips.

Raman spectroscopy and PL measurements on the as-exfoliated MoS_2 and after the high- κ dielectric deposition have been executed by a Horiba HR-Evolution micro-Raman system with a confocal microscope ($100\times$ objective) and a laser excitation wavelength of 532 nm. A grating of 1800 lines/mm was employed for the Raman measurements in a range between $150\text{-}650 \text{ cm}^{-1}$, while a grating of 600 lines/mm was used for PL measurements in a range between $10\text{-}5500 \text{ cm}^{-1}$.

Finally, DFT calculations were performed in order to assess the structural and electronic properties of the $\text{MoS}_2/\text{Au}(111)$ interface using the Quantum Espresso software package [38] with the van der Waals exchange-correlation functional of Hamada [39]. The modelled system comprised a single MoS_2 layer relaxing on an $\text{Au}(111)$ bilayer. Due to the mismatch between the lattice parameters of the two parts of the heterostructure, a laterally strained $\text{Au}(111)$ bilayer model was constructed in

order to acquire the calculated equilibrium lattice parameters of the MoS₂ sheet (3.167 Å). Convergence was obtained with a plane-wave cut-off kinetic energy of 50 Ry and an augmented charge density cut-off of 400 Ry, using a (12×12×2) Monkhorst-Pack grid for the sampling of the Brillouin zone [40]. A vacuum space of 20 Å perpendicular to the MoS₂/Au(111) interface was inserted in order to avoid spurious interactions between the periodic replicas of the system. Calculations for the adsorption energy of ALD precursors (H₂O, TMA) on freestanding MoS₂ and the MoS₂/Au heterostructure were performed in (3×3) supercells with the same structural and convergence parameters as before, using a (4×4×2) Monkhorst-Pack grid for the sampling of the Brillouin zone.

3. Results and discussion

3.1 Nanoscale structure, strain and doping of 1L-MoS₂ exfoliated on gold

The morphological, structural and vibrational properties of the as-exfoliated MoS₂ membranes on the Au/Ni/SiO₂ stack were preliminary assessed by the combination of optical microscopy, AFM, micro-Raman and high resolution TEM/EDS analyses. Fig.1(a) shows an optical image of the sample surface, where 100 μm-wide regions covered by 1L-MoS₂ exhibit a slightly darker contrast as compared to bare Au regions. The presence of smaller size multilayer MoS₂ areas, with a dark violet contrast can be also observed in the image. Fig.1(b) shows a high-magnification AFM morphology collected at the boundary region between the 1L-MoS₂/Au and a bare Au area. The roughness of the Au surface is due to the grain structure of the metal film deposited by sputtering, and the MoS₂ membrane seems to be very conformal to the morphology of underlying Au. To obtain quantitative information on the thickness and root mean square roughness of 1L-MoS₂ with respect to the Au surface, the histogram of the height values was extracted from this morphological analysis and reported in Fig.1(c). This distribution exhibits two well separated peaks, associated to the bare Au and 1L MoS₂/Au areas, which could be fitted by Gaussian contributions with very similar standard deviations ($\sigma_{\text{Au}}=0.25$ nm and $\sigma_{\text{MoS}_2/\text{Au}}=0.28$ nm), indicating a conformal coverage of MoS₂ on Au. Furthermore the separation between these peaks ($t=0.64$ nm) is very close to the typically reported thickness of 1L-MoS₂ evaluated by AFM analyses [17].

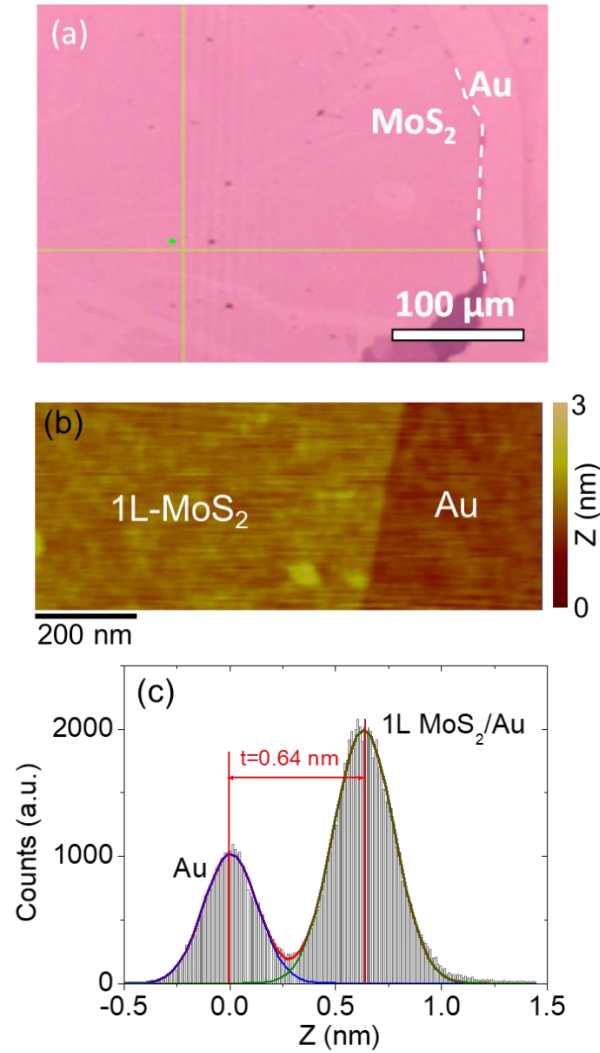


Figure 1 (a) Optical image of the MoS₂ membrane exfoliated on Au, where the brighter contrast correspond to bare Au regions, a slightly darker contrast to extended areas covered by 1L-MoS₂, and the dark violet contrast to areas with multilayer MoS₂. (b) AFM topography in a region at the boundary between 1L-MoS₂/Au and bare Au. (c) Histogram of the height values extracted from the AFM image, and fit with two Gaussian contributions. The root mean square roughness of the two regions and the thickness of 1L-MoS₂ ($t=0.64$ nm) with respect to the Au substrate were evaluated from this analysis.

Fig.2(a) shows a typical Raman spectrum collected on the 1L-MoS₂ membrane on Au. Noteworthy, the measured separation $\Delta\omega \approx 21.2$ cm⁻¹ between the out-of-plane (A_{1g}) and in-plane (E_{2g}) vibrational modes is larger than the typically reported values (from 18 to 19 cm⁻¹) for 1L-MoS₂ on commonly used insulating substrates (such as SiO₂) [41]. This discrepancy for gold-supported 1L-MoS₂ has been attributed to the combined effect of a tensile strain (causing a red-shift of the E_{2g} peak) and of a p-type doping (causing a blue-shift of the A_{1g} peak) [23,42].

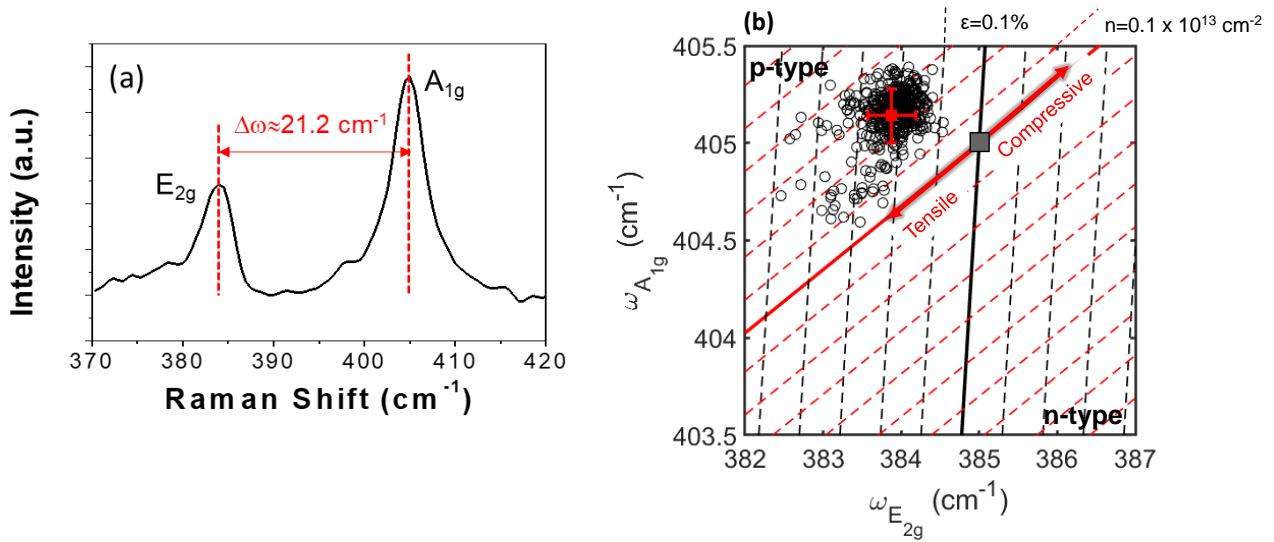


Figure 2 (a) Typical Raman spectrum of 1L-MoS₂ exfoliated on Au, with the indication of the characteristic in-plane (E_{2g}) and out-of-plane (A_{1g}) vibrational modes and their separation $\Delta\omega \approx 21.2$ cm⁻¹. (b) Correlative plot of the $\omega_{A_{1g}}$ and $\omega_{E_{2g}}$ peak frequencies extracted from an array of Raman spectra measured at different positions on the 1L-MoS₂/Au sample.

The Raman spectra reported in Fig.2(a) are similar to the ones reported in some recent papers [30,32,33,36]. On the other hand, they differ from the spectra reported in other works [34,35], which showed an anomalous splitting in two components of the A_{1g} peak (mainly related to MoS₂ doping), and a large redshift of the E_{2g} peak (mainly related to MoS₂ strain). The A_{1g} peak splitting was ascribed in Ref. [34] to a non-conformal morphology of the exfoliated MoS₂ on the Au surface, with a large density of nanoscale regions where the membrane is suspended (i.e. not directly in contact with the Au surface). This resulted in the coexistence of doped and undoped MoS₂ patches, which are reflected in the two components of the A_{1g} peak. The large redshift of the E_{2g} peak is due to the large strain of MoS₂, probably related to this peculiar morphology. Hence, the main differences between our MoS₂/Au samples and those investigated in these recent literature works arise from a more conformal morphology of MoS₂ on the Au surface.

The MoS₂ strain and doping can be quantitatively evaluated by a correlative plot of the A_{1g} vs E_{2g} wave-numbers, as illustrated in Fig.2(b). Here, the open points represent the experimental ($\omega_{E_{2g}}$, $\omega_{A_{1g}}$) values measured on an array of 21×21 laser positions in a 5μm×5μm area of 1L-MoS₂ surface, whereas the red (black) continuous lines are strain (doping) lines, illustrating the theoretical relations in the case of an ideally undoped (unstrained) monolayer of MoS₂. The literature values of the E_{2g} and A_{1g} peaks' frequencies measured on a suspended monolayer MoS₂ ($\omega_{E_{2g}}^0=385$ cm⁻¹, $\omega_{A_{1g}}^0=405$ cm⁻¹) [43] were taken as the origin in the plot. In fact, freestanding MoS₂ can be considered

as a good approximation of the ideal unstrained and undoped monolayer, since the effects of the interaction with the substrate are removed. From this plot, a tensile strain ranging from $\varepsilon \approx -0.1\%$ to $\varepsilon \approx -0.3\%$, and a p-type doping ranging from 0.1×10^{13} to $0.4 \times 10^{13} \text{ cm}^{-2}$ can be observed. Obviously, these are averaged values on the micrometer area probed by the laser spot. It is expected that local values of strain exhibit larger variations at the nanoscale, depending on the local morphological/structural properties of MoS₂/Au interface.

To get a deeper insight on these aspects, the structural properties of the MoS₂/Au heterointerface have been investigated by cross-sectional TEM/STEM analyses. Fig.3(a) shows a low-magnification TEM analysis of the whole MoS₂/Au/Ni/SiO₂ stack, from which the thickness and the grain size of the Ni wetting layer and of the Au films can be directly deduced. The presence of the 1L-MoS₂ on the Au surface can be also observed in this image, and it is further confirmed by the high magnification EDS chemical maps of Mo, S and Au distributions, reported in Fig.3(b), (c) and (d), respectively. Interestingly, such nanoscale analysis confirms that the ultra-thin MoS₂ membrane generally follows the morphology of Au grains, appearing to be suspended in some regions, typically corresponding to Au grain boundaries (see white arrow in Fig.3(a)).

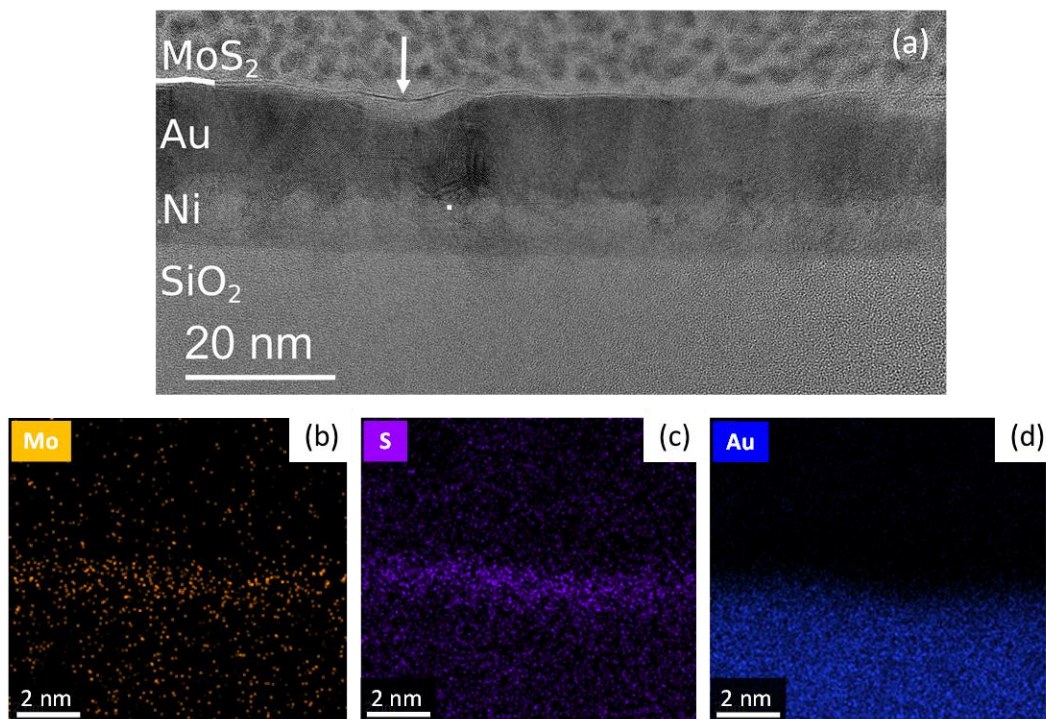


Figure 3: (a) Low magnification TEM analysis of the monolayer MoS₂ membrane on the Au/Ni/SiO₂ stack. EDS maps of Mo (b), S (c), Au (d) acquired on the magnified MoS₂/Au region.

Atomic resolution information on the 1L-MoS₂/Au interface structure were obtained by aberration corrected STEM analyses in the HAADF mode. In this imaging mode, based on the collection of

electrons scattered at high angle, atomic columns of elements with high atomic number Z , such as Au and Mo exhibit a brighter contrast. Fig.4(a) and (c) show two representative analyses showing the MoS₂ residing on the atomic terraces and steps exposed by the gold grains.

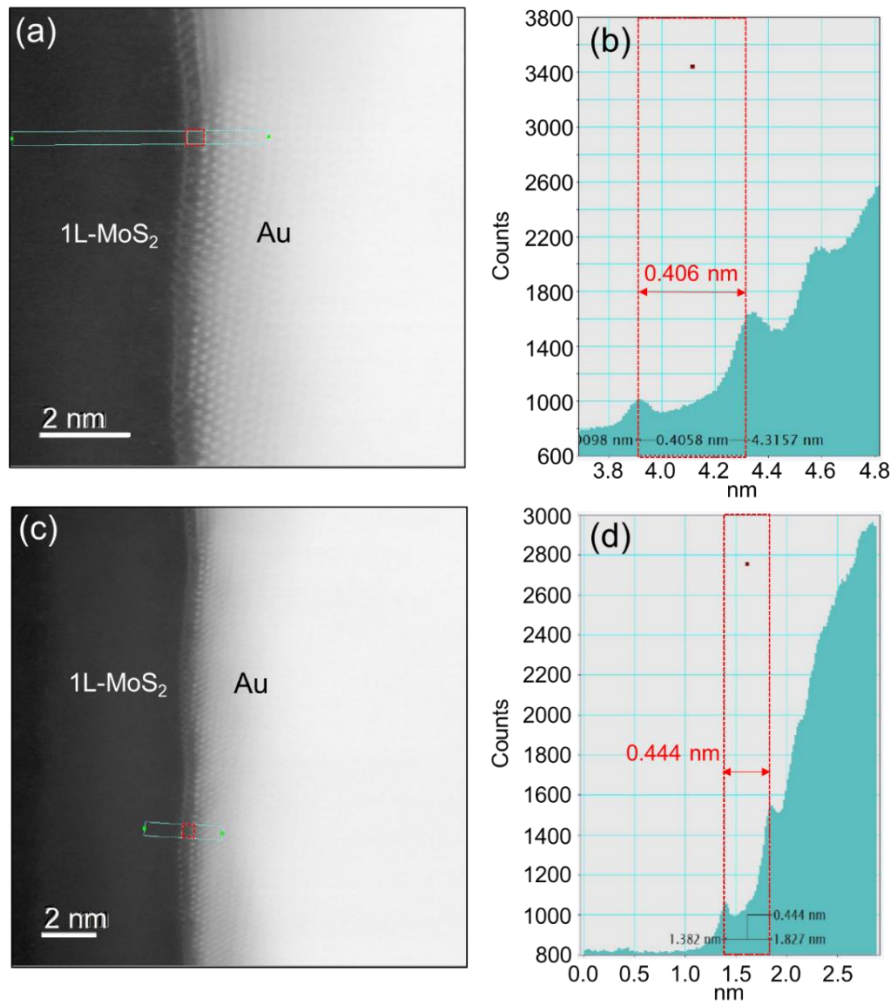


Figure 4: (a,c) Aberration corrected STEEM/HAADF analyses of 1L-MoS₂/Au interface. (b,d) Intensity line profiles, from which the atomic distance between the Mo atoms of the MoS₂ membrane and the topmost Au atoms was evaluated.

The atomic distances ($d_{\text{Mo-Au}}$) between the Mo atoms of the MoS₂ layer and the topmost Au atoms was evaluated from the intensity linescans, as illustrated in Fig.4(b) and (d). A variability of $d_{\text{Mo-Au}}$ from $\sim 4.0 \pm 0.1 \text{ \AA}$ to $\sim 4.5 \pm 0.1 \text{ \AA}$, depending on the local configuration of Au planes, is observed, which correspond to S-Au interatomic distances ($d_{\text{S-Au}}$) of 2.4-2.9 \AA . These values are indeed lower than the S-Au distance of 3.5 \AA obtained by Velický et al. [32], starting from a $d_{\text{Mo-Au}}$ value of $5.1 \pm 0.3 \text{ \AA}$, measured by STEM. The origin of the smaller $d_{\text{Mo-Au}}$ distances obtained in our work may be related to a more conformal adhesion of MoS₂ to the Au surface, as confirmed by AFM morphologies

in Fig.1(b) and (c), showing similar roughness values on MoS₂/Au and bare Au surfaces, and by Raman spectra in Fig.2(a), without splitting of the A_{1g} peak. We want also to point out that, although the d_{S-Au} distances obtained in our work indicate a stronger S-Au interaction than a common vdW bond, they are still higher than the expected d_{S-Au} distance (2.2 Å) for a S-Au covalent bond [32]. Furthermore, these d_{S-Au} distances are lower than the interlayer vdW spacing d_{S-S} of 3.0 Å between S atoms of MoS₂ layers in bulk MoS₂, which is reasonable to explain monolayer MoS₂ exfoliation of Au.

3.2 DFT calculations of an ideal MoS₂/Au system and its reactivity to ALD precursors

In order to obtain a better insight on the fundamental structural/electronic properties of the MoS₂/Au(111) system, we have computed the equilibrium distance and binding energy of this interface using DFT calculations. Upon structural relaxation, the coupled system largely preserved the structural characteristics of the respective pristine structures, indicating a van der Waals heterostructure (see Fig. 5). The obtained Mo-Au equilibrium distance of 4.28 Å is in line with the experimental measurements, whereas a strong binding energy per interface atom was calculated (~0.26 eV), implying a rather strong attachment for a van der Waals system. This aspect explains the successful exfoliation of ultra-thin MoS₂ membranes through pressing of molybdenite stamps on the Au surface and the resulting acquisition of the Au surface morphology from the MoS₂ layers. Electronically (Fig. 5a), the interface is characterized by a finite density of states around the Fermi level due to the presence of states deriving from the Au substrate. On the other hand, the MoS₂ layer preserves the direct nature of its bandgap for monolayer structures at the *K* Brillouin zone point (Fig. 5b), showing however a partial hybridization of its Mo 4d orbitals with Au(111) surface states.

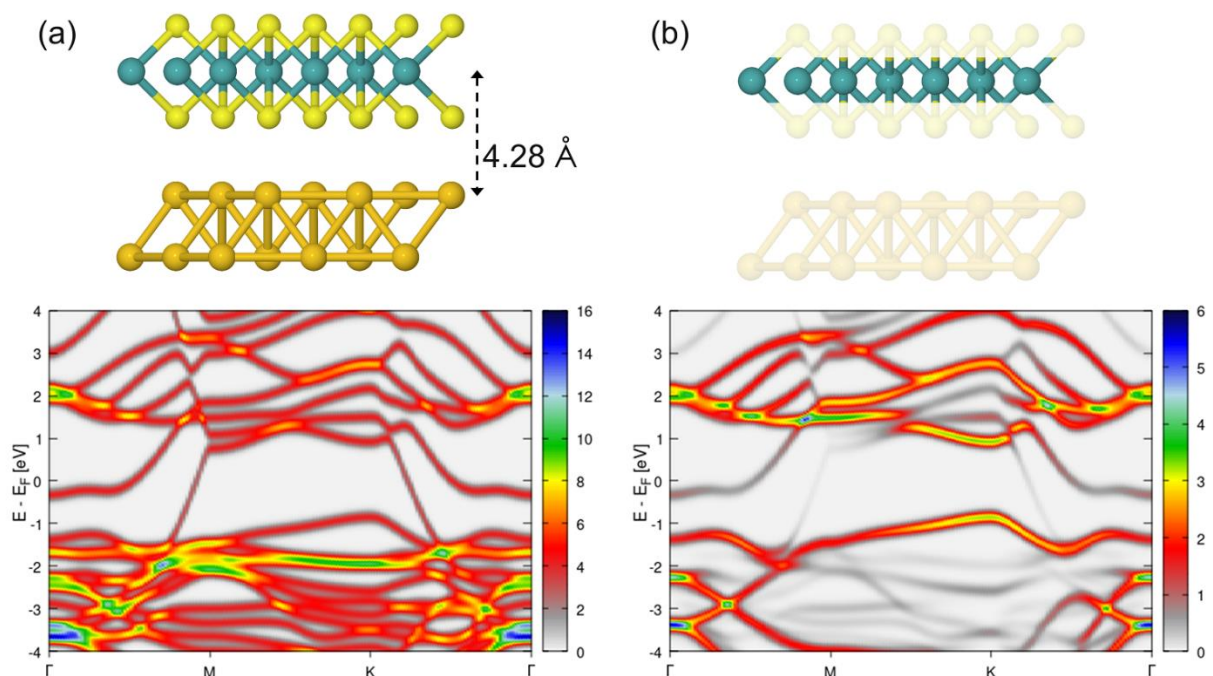


Figure 5: Structure and electronic properties of the MoS₂/Au(111) interface showing the (a) the total k-resolved projected density of states, and (b) the partial k-resolved projected density of states only for Mo 4d orbitals.

We have thereon focused on the ALD deposition process and calculated the adsorption energy of all ALD precursors (H₂O, TMA, TDMAHf) on the MoS₂/Au system, comparing these values with respective ones obtained for the interaction between the same molecules and freestanding MoS₂. Fig.S1 of the Supporting Information shows the optimized configurations for the adsorption of (a) H₂O, (b) TMA (monomer), and (c) TDMAH molecules on the MoS₂/Au(111) surface, based on DFT calculations. The results of this simplified model for the 1L-MoS₂/Au system showed that the Au substrate slightly improves the adsorption of the TDMAHf precursor on MoS₂ but only marginally affects the adsorption of the H₂O and TMA molecular species (see Tab.1). This indicates that the enhanced ALD nucleation on Au-supported MoS₂ should be mainly related to morphological (e.g., surface curvature, bound and unbound MoS₂ regions) and associated structural modifications (e.g., strain or deformation of the MoS₂ layer), as shown by the previous characterizations of the MoS₂/Au system. To this end, a detailed experimental analysis on the nucleation process should better clarify the studied ALD growth mechanism.

Table 1: Adsorption energy (in eV) calculated for an H₂O, TMA (monomer) and TDMAHf molecule on free-standing MoS₂ and MoS₂ supported on an Au(111) substrate.

	H ₂ O	TMA (monomer)	TDMAHf
MoS ₂	-0.11	-0.47	-0.46
Au(111)/MoS ₂	-0.12	-0.48	-0.52

3.3 Nucleation and growth of Al₂O₃ and HfO₂ on MoS₂/Au

In this section, the nucleation and growth of HfO₂ and Al₂O₃ on the MoS₂/Au system has been investigated for different number of ALD cycles. The coverage degree of the MoS₂ surface by both high-κ dielectrics has been evaluated by tapping mode AFM. Fig.6 displays the comparison of AFM-morphology (a) and phase (b) of 40 ALD cycles HfO₂ on MoS₂/Au, chosen as representative sample. The morphological map indicates an incomplete coverage of MoS₂ surface by the growing HfO₂ grains. This is further confirmed by the phase map, which is known to be sensitive to the surface composition. In particular, the violet color in the phase image coincides with HfO₂ covered regions, as shown in the morphological image, whereas the green phase contrast is associated to the uncovered areas. In the following, the AFM phase maps have been used to evaluate the ALD coverage degree as a function of the number of cycles for both Al₂O₃ and HfO₂.

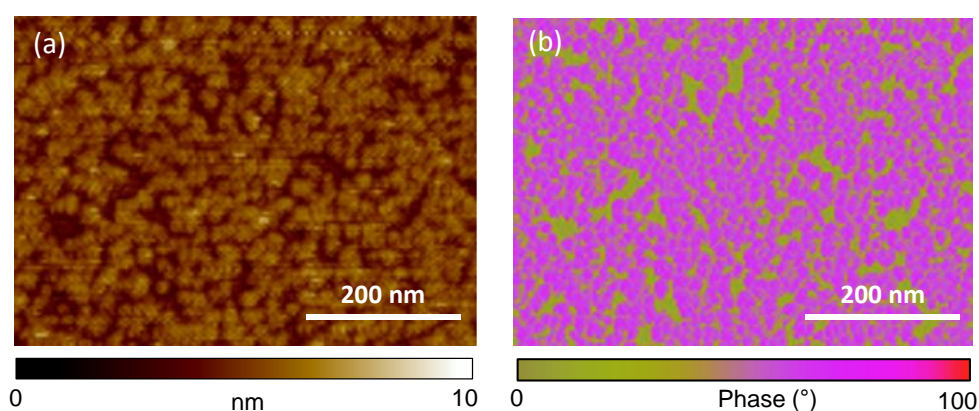


Figure 6: Comparison of AFM morphology (a) and phase (b) of 40 ALD cycles HfO₂ on MoS₂/Au

Fig. 7 compares the phase maps of Al₂O₃ (a) and of HfO₂ (b) grown on 1L- MoS₂ after 10, 40, 80 and 120 ALD cycles. As previously noted, the violet and green regions indicate the covered and

uncovered MoS₂ surface by the high- κ dielectrics, respectively. The evolution of surface percentage coverage, calculated from the phase maps, is reported in Fig. 7(c). It can be observed how, after only 10 cycles, Al₂O₃ covers 50 ± 3 % of the MoS₂ surface, whereas it reaches 93 ± 2 % coverage after 40 cycles, and 100% after 80 and 120 cycles, as reported in our previous work [17]. Differently, the growth evolution of HfO₂ appears to be slower during the initial deposition cycles. In particular, it exhibits a coverage degree of about 15 ± 3 % after 10 cycles and 70 ± 3 % after 40 cycles. An almost complete layer (97 ± 3 %) is obtained after 80 cycles and a 100 % coverage after 120 cycles.

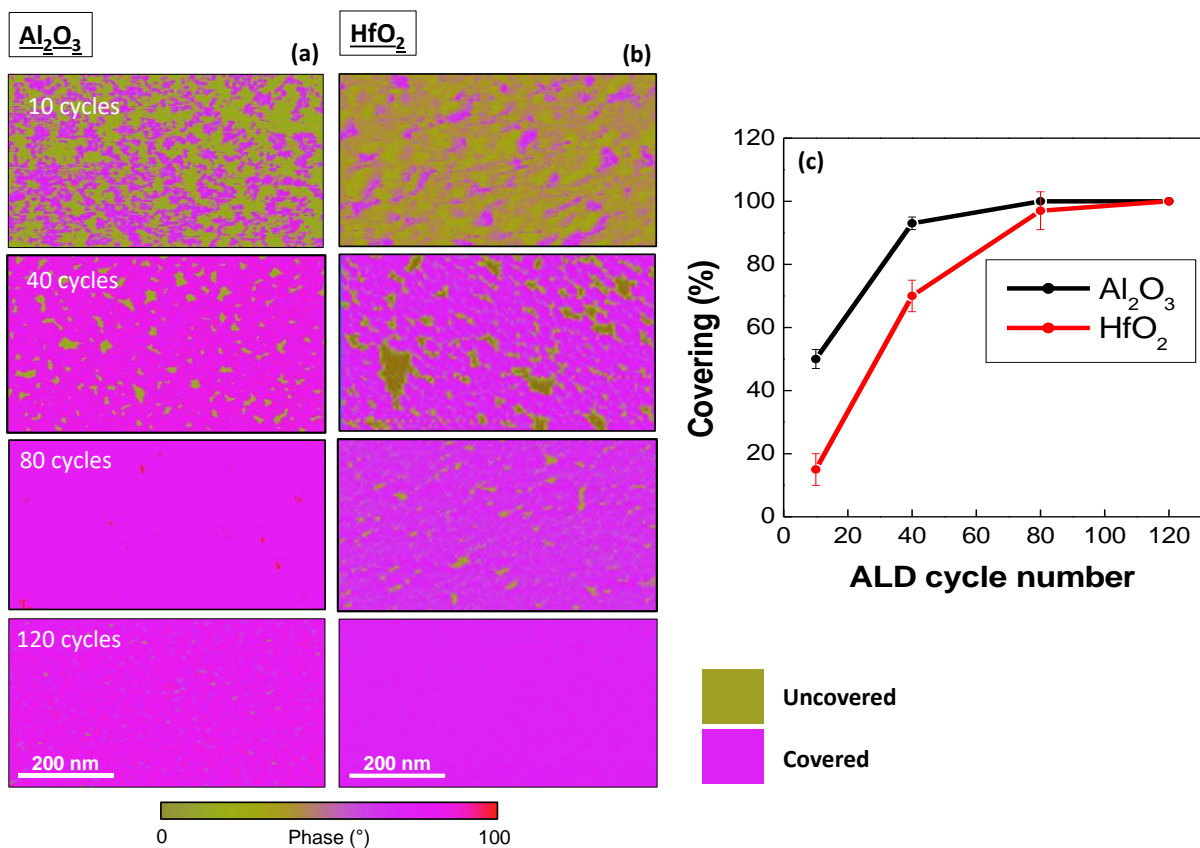


Figure 7: AFM phase maps after 10, 40, 80 and 120 ALD cycles of deposition Al₂O₃ (a) and HfO₂ (b) on monolayer-MoS₂/Gold. The green contrast represents the uncovered MoS₂/Gold by high- κ dielectrics. Conversely, the magenta contrast represents the covered MoS₂/Gold by high- κ dielectrics. The coverage degree between the Al₂O₃ and HfO₂ ALD deposition is graphically compared in (c).

To get further insight in the nucleation mechanism of the two high- κ insulators on the Au-supported 1L-MoS₂, the grain size distributions in the early stages of ALD deposition have been investigated in detail. Fig.8(a) and (d) show the AFM morphologies of Al₂O₃ and HfO₂ after the 40-cycles ALD processes. To precisely evaluate the island sizes, the grain boundaries have been highlighted by image

processing, as displayed in Fig.8(b) and (e). Therefore, the histograms of grain diameters have been evaluated, as shown in Fig.8(c) and (f).

Differently than the layer-by-layer ALD growth, typically reported on common semiconductor substrates and resulting in the formation of conformal and flat dielectric films, a 3D-growth mode is observed on the surface of van der Waals layered materials, due to the weak interaction between precursors and substrate. In this case the growth process evolves by the initial islands formation and their subsequent coalescence toward a full layer. In this regard, recent works have proposed some models to describe 3D-growth mechanisms depending on the main deposition parameters, the nature of deposited material and substrate, and their interactions [44,45]. In general, these models take into account: (i) the cyclic deposition of atoms on the surface of the substrate and of the islands formed during previous ALD cycles; (ii) the diffusion/aggregation of the deposited atoms on the substrate to form new islands; (iii) the diffusion and coalescence of islands (dynamic coalescence). In this context, Grillo et al. [44,45] showed how the peculiar shape of the island-size distribution measured at a certain stage of the ALD process provides information on the specific growth mechanism.

Hence, we analyzed the island maps and the size distributions, reported in Fig.8, to draw some conclusion about the growth mechanism of Al_2O_3 and HfO_2 on the 1L- MoS_2/Au system. We found that the Al_2O_3 morphology (Fig.8 (a)) is formed by nanometric islands, densely arranged, and with a modest uncovered portion of MoS_2 (~ 7 %) as shown in Fig.8 (b). Moreover, the distribution of Al_2O_3 island's diameters, reported in Fig.8(c), exhibits a bimodal shape fitted with two Gaussian contributions, i.e. a narrow peak at ~7 nm and a broader peak at ~12 nm. Differently, the HfO_2 morphology is formed by larger islands and a larger uncovered fraction of MoS_2 (30 %), as shown in Fig. 8 (d), (e). The distribution of HfO_2 island's diameters (Fig. 8 (f)) also exhibits a bimodal shape, with a narrow peak at ~7 nm and a broader peak at ~20 nm. The small-size peak is attributable to the new atoms arriving on the surface of the substrate. The large-size peak is correlated to the growing islands as a result of new deposition, diffusion, and coalescence. Hence, the bimodal shape, obtained for both high- κ , is an indication of a nucleation mechanism involving a cyclic deposition of materials both on bare substrate and on preexisting islands, as well as a dynamic coalescence. However, HfO_2 exhibits a broader large-size peak, shifted toward 20 nm, than Al_2O_3 . The formation of larger grains can be correlated to a lower diffusivity in the case of HfO_2 due to its bulky metalorganic precursor. Since diffusion processes help the 2D-growth, when they are disadvantaged, a high number of cycles are required to reach the complete covering. This mechanism can be the explanation of the delay of HfO_2 process than Al_2O_3 . Hence, although DFT calculations predicted a slightly better adsorption of

single TDMAHf molecules on MoS₂/Au (Table 1), the steric hindrance effect due to bulky structure of this precursor represents the limiting factor for HfO₂ nucleation.

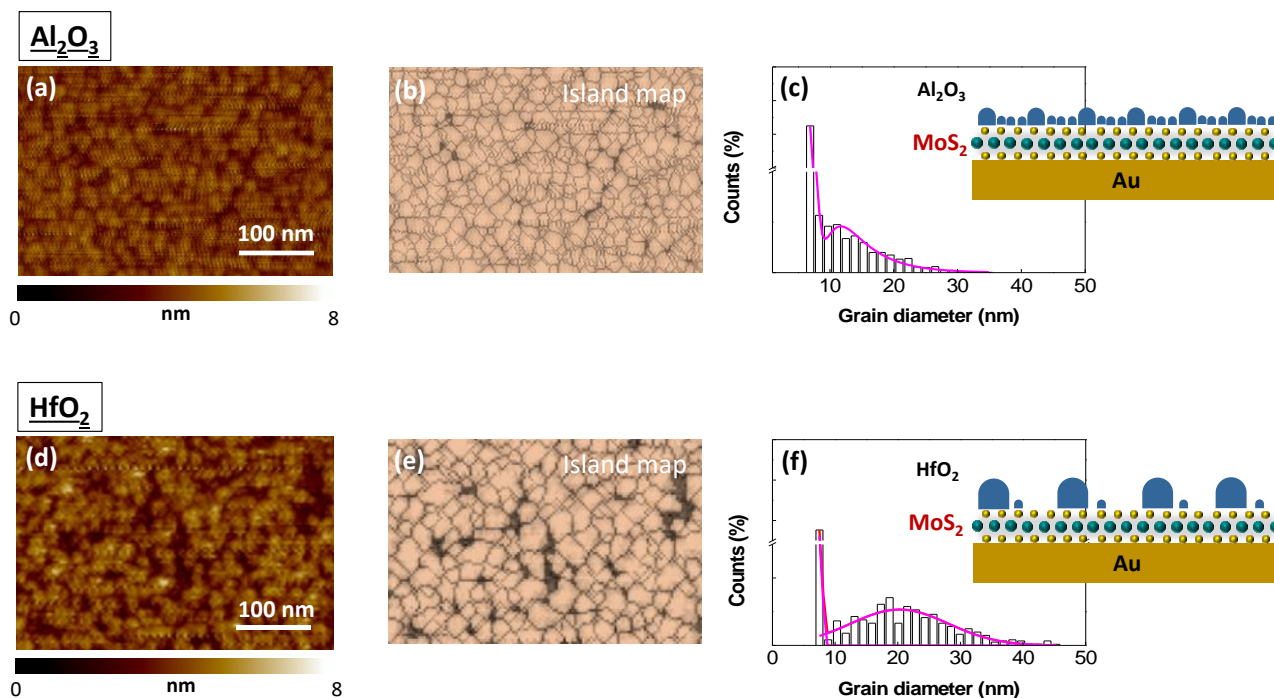


Figure 8: High-magnification AFM morphology of Al₂O₃/MoS₂ (a) and HfO₂/MoS₂ (d) after 40 ALD cycles. Island maps of Al₂O₃/MoS₂ (b) and HfO₂/MoS₂ (e) after 40 ALD cycles reproduced by the AFM morphologies (a) and (d). Distributions of the islands diameters for Al₂O₃/MoS₂ (c) and HfO₂/MoS₂ (f) referred to the islands map of (b) and (e). The schematics superimposed on (c) and (f) are illustrates the nucleation mechanism of Al₂O₃ and HfO₂ on MoS₂, respectively.

3.4 Insulating properties of the high-κ layers

The electrical quality of the high-κ layers has been further evaluated by conductive-AFM analyses. In particular, by scanning the metal-coated tip across the step between the high-κ grown on MoS₂ and the underlying Au substrate (as illustrated in Fig.9 (a)), we acquired the topographies (Fig.9 (b), (d)) as well as the current maps of the same region (Fig.9 (c), (e)). From the measured steps in the height line-scans of the Al₂O₃/MoS₂/Au (insert of Fig. 9 (b)) and HfO₂/MoS₂/Au (insert of Fig. 9 (d)) and after subtracting the monolayer MoS₂ thickness (~0.64 nm), the thicknesses of the two dielectrics after 80 ALD cycles were estimated as ~3.6 nm and ~3.1 nm, respectively. These measured thickness were about half those expected based on the growth rate previously evaluated on Si (0.88 Å/cycle). This clearly indicates that the ALD growth on the MoS₂/Au surface is much slower than on Si, especially in the early stages of the deposition. Of course, this is a consequence of the lack of out-of-plane bonds (which act as active sites of nucleation) on the MoS₂ surface, differently than on the Si surface. Despite this delayed growth, it is important noting that a uniform nucleation is obtained on

Au-supported MoS₂, resulting in the formation of homogeneous dielectric films after 80 cycles. A completely different scenario, i.e. a very inhomogeneous dielectric film, is typically observed for similar deposition conditions on MoS₂ supported by an insulating substrate (such as SiO₂ or Al₂O₃ on silicon) [17].

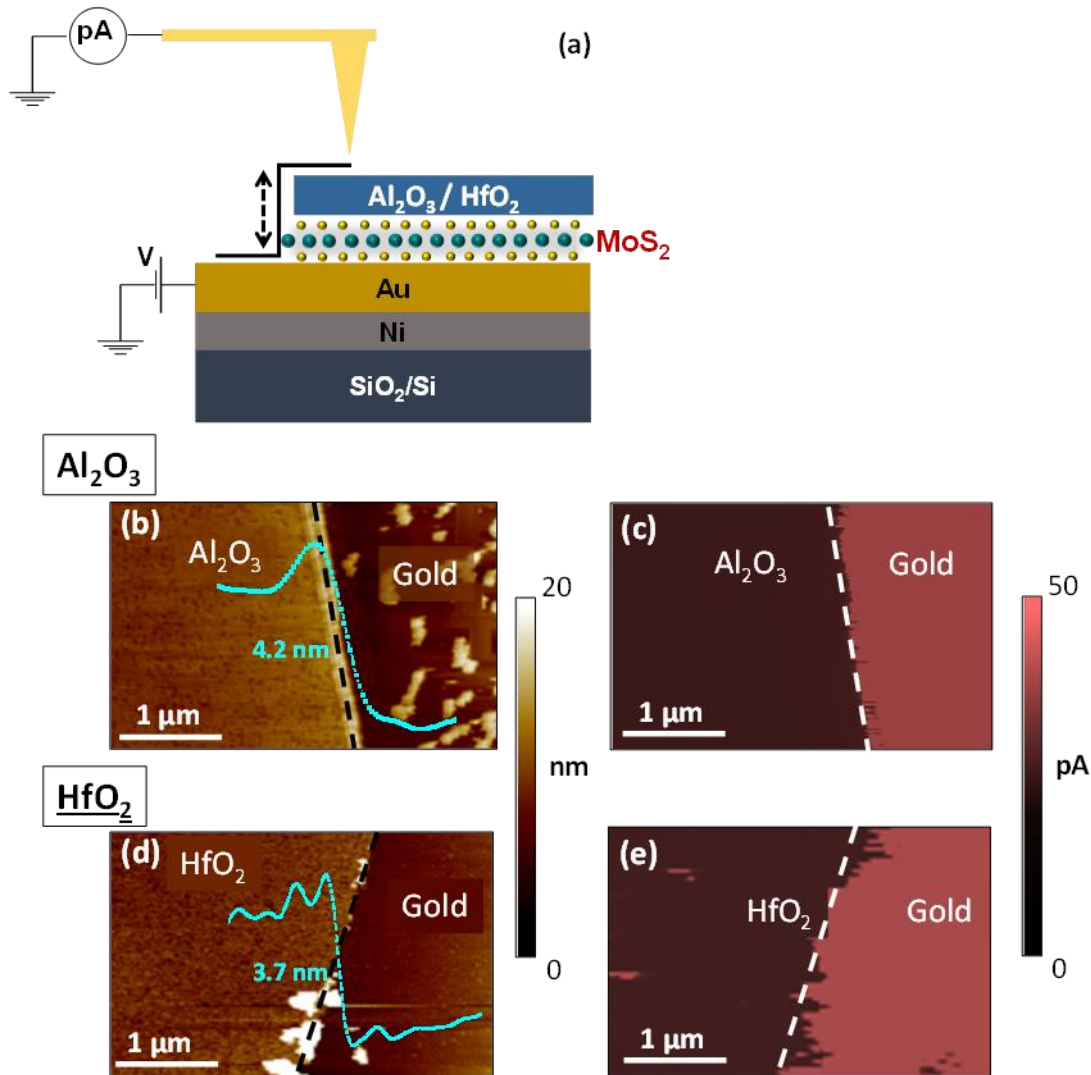


Figure 9: Schematic of the step between the high- κ (Al₂O₃ or HfO₂)/ MoS₂ and the underlying gold and with the circuit used for conductive-AFM measurements (a). AFM image of the step between Al₂O₃/MoS₂ (b) and HfO₂/MoS₂ (e) on Au after 80 ALD cycles. Height line-scans of the Al₂O₃/MoS₂/Au and HfO₂/MoS₂/Au from which the thickness of the dielectrics have been determined are reported as insert in (b) and (c), respectively. Current maps of the step between Al₂O₃/MoS₂ (c) and HfO₂/MoS₂ (e) on Au after 80 ALD cycles, acquired on the same regions of (b) and (d), with a bias $V=3$ V.

By applying a bias of 3 V between the tip and the gold substrate, it is possible to observe in Fig.9 (c) a very homogeneous insulating behavior for the Al₂O₃ on MoS₂, and the expected conductive behavior for gold. Under the same applied bias conditions, the HfO₂ layer grown on MoS₂ (Fig.9 (f))

exhibits good insulating performances, with the presence of some isolated current spots, which can be associated with less dense regions of the HfO₂ layer. This phenomenon is observed mainly on the HfO₂ layer probably due to a more inhomogeneous nucleation than the Al₂O₃ during the early stages. A current map has been also acquired at the same bias of 3V on the HfO₂ film deposited on MoS₂/Au by 120 ALD cycles. As shown in Fig.S2(a) of the Supporting Information, uniform insulating properties (without current spots) and a lower current level is observed, due to the higher thickness (~ 4.7 nm) of the HfO₂ film.

3.5 Impact of Al₂O₃ and HfO₂ deposition on the strain, doping and optical emission of 1L-MoS₂

Micro-Raman spectroscopy analyses have been performed to investigate the effect, in terms of strain and doping, of the high-k deposition on 1L-MoS₂. In order to correctly estimate these effects, Raman characterization has been performed on the samples that present a complete dielectric layer. Thus, Al₂O₃ and HfO₂ layers grown using 80 cycles have been investigated.

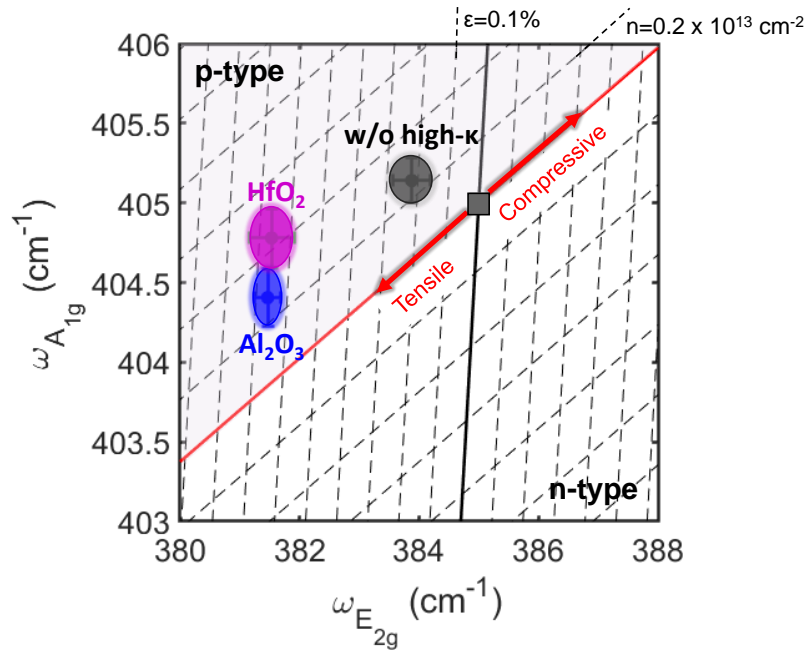


Figure 10: Correlative plot of the A_{1g} versus E_{2g} of the Raman spectra acquired on monolayer MoS₂ on Gold without high-κ (black circle) and of the same covered with 80 ALD cycles of Al₂O₃ (blue circle) and HfO₂ (magenta circle), allowing to estimate the type and the average values of strain and doping of monolayer MoS₂. The spacing of the dashed lines, parallel to the ideal strain and doping lines, is associated with carrier density changes of $0.2 \times 10^{13} \text{ cm}^{-2}$ and strain changes of 0.1%, respectively.

In Fig.10, the strain and doping of MoS₂ before and after the ALD processes have been estimated by the correlative analysis of A_{1g} versus E_{2g} peak frequencies, similarly to Fig.2(b). In Fig.10, the black circle indicates the range of experimental data points measured on 1L-MoS₂/Au before the ALD

processes. It is characterized by an average tensile strain of $\varepsilon \approx 0.21\%$ and p-type doping of $0.25 \times 10^{13} \text{ cm}^{-2}$. Differently, the blue ellipse, referred to $\text{Al}_2\text{O}_3/\text{MoS}_2$ system, indicates an average tensile strain of $\varepsilon \approx 0.65\%$ and p-type doping of $0.25 \times 10^{13} \text{ cm}^{-2}$. While, the magenta ellipse, related to $\text{HfO}_2/\text{MoS}_2$ sample, exhibits an average tensile strain of $\varepsilon \approx 0.65\%$ and p-type doping of $0.45 \times 10^{13} \text{ cm}^{-2}$. It is obvious the strong impact of both high-k on strain properties of MoS_2 , which changes from $\varepsilon \approx 0.21\%$ to $\varepsilon \approx 0.65\%$, before and after the ALD process, respectively. Moreover, Al_2O_3 layer causes a negligible effect on the MoS_2 doping, which remains unchanged ($0.25 \times 10^{13} \text{ cm}^{-2}$). Conversely, HfO_2 is responsible of a higher p-type doping of $0.45 \times 10^{13} \text{ cm}^{-2}$. This higher doping can be due to a higher density of charged defects at the $\text{HfO}_2/\text{MoS}_2$ interface, due to the less efficient nucleation during the early growth stage of HfO_2 than Al_2O_3 .

In the final part of this paper, the effects of Al_2O_3 and HfO_2 deposition on the photoluminescence (PL) spectra of 1L- MoS_2 is investigated. The interaction between MoS_2 and the Au substrate is well known to cause a total [34] or partial quenching [33,36] of the PL of monolayer MoS_2 , as compared to MoS_2 residing on insulating substrates. In our previous papers [23,42] on 1L- MoS_2/Au samples, we have observed that the PL intensity is significantly quenched (but not totally suppressed), and the main PL peak is red-shifted compared to 1L- MoS_2 on an Al_2O_3 substrate. The origin of PL quenching in the 1L MoS_2/Au system can be ascribed to different factors, such as the preferential transfer of photoexcited charges to the Au substrate, and a large strain of the MoS_2 membrane causing a modification of the energy bandstructure [46]. In our case, the 1L- MoS_2 is nearly conformal to the underlying Au, but its strain is $\varepsilon \approx -0.3\%$, as shown in Fig.2(b). Probably this allows us to measure a PL spectrum, although partially quenched.

In Fig. 11, the black dots represent the PL spectra of bare monolayer MoS_2 on Au (a) and after 80 ALD cycles, resulting in the formation of continuous films of Al_2O_3 (b) and HfO_2 (c). A significant reduction (from ~2-4 times) of the main PL peak intensity and a modification of the shape of the spectra can be observed after MoS_2 encapsulation with Al_2O_3 and HfO_2 . Such lowering of the PL intensity can be correlated, in the first approximation, to the increase of tensile strain in the MoS_2 membrane observed by Raman data in Fig.10, coherently with previous reports [17,43]. To get further insights on the differences between the Al_2O_3 and HfO_2 coated samples with respect to the bare 1L- MoS_2/Au , a deconvolution analysis of the PL spectra was carried out in Fig.11(a)-(c). All the experimental data can be well fitted by three different peaks, associated to the excitonic contributions A (blue line) and B (magenta line), and to the trionic contribution A^- (green line), respectively [23]. This analysis revealed a significant reduction of the intensity ratio between the trionic (A^-) and the excitonic (A) peaks, from ~1.8 on the bare 1L- MoS_2 to ~0.8 and ~0.9, after the deposition of Al_2O_3 and HfO_2 , res

pectively. Recently, Lin et al. [47] demonstrated a decreasing trend of the A^-/A intensity ratio in the PL spectra of 1L-MoS₂ with the effective dielectric constant of the surrounding environment. Hence, in addition to overall quenching of the PL signal due to the increased compressive strain, the encapsulation of 1L-MoS₂ with the high-k dielectric films modifies the relative intensities of A^- and A contributions, resulting in a change in the shape of the PL spectra.

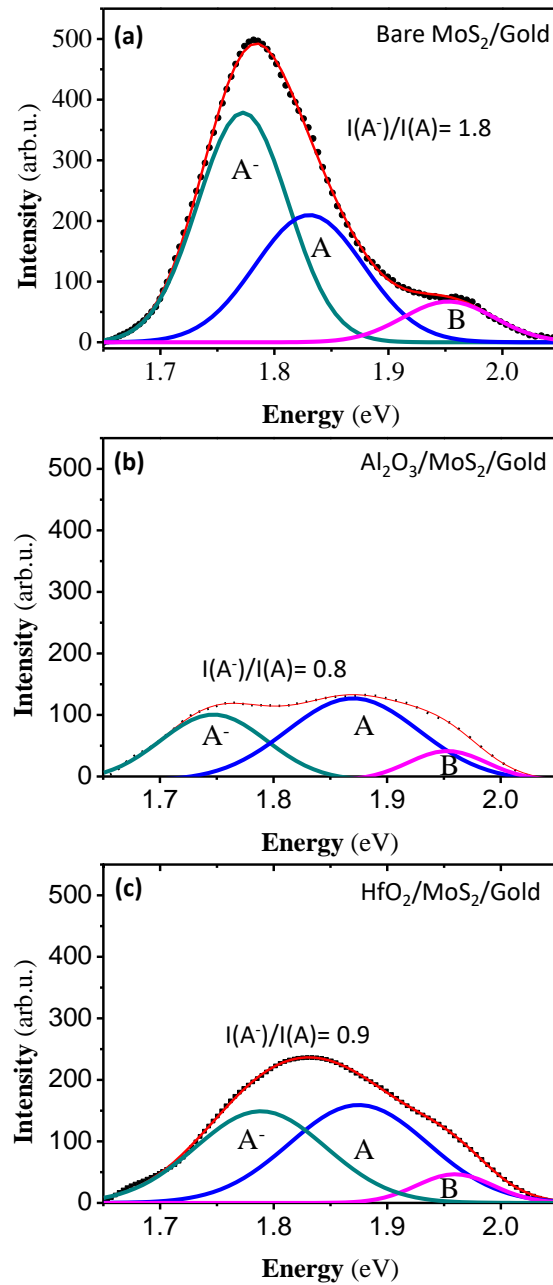


Figure 11: Micro-PL spectra on the bare 1L-MoS₂/Au (a) and after 80 ALD cycles of Al₂O₃ (b) and HfO₂ (c). The deconvolution of the PL peak results in three different contributions: the trion peak A^- , the exciton A, the exciton B.

4. Conclusions

In conclusion, we have demonstrated the direct thermal ALD of two technologically relevant high- κ insulators (Al_2O_3 and HfO_2) on gold-supported monolayer (1L) MoS_2 , providing an insight on the mechanisms ruling the nucleation in the early stages of the ALD process. The strain, doping, and morphology of the large area 1L- MoS_2 exfoliated on sputter-grown Au/Ni films have been preliminarily assessed by a complete multiscale characterization. Micro-Raman mapping demonstrated a tensile strain and p-type doping distribution on MoS_2 , induced by the interaction with the substrate. Nanoscale resolution morphological/structural analyses by AFM/TEM showed that the MoS_2 membrane is almost conformal to the Au nanocrystals topography, with some locally detached regions. Furthermore, atomic scale resolution STEM demonstrated a variability from ~ 4.0 to ~ 4.5 Å in the Mo-Au atomic distance between 1L- MoS_2 and the topmost Au atoms, depending on the local configuration of Au nanocrystals planes. *Ab initio* DFT calculations of a free-standing MoS_2 and an ideal (unstrained) $\text{MoS}_2/\text{Au}(111)$ system showed a significant influence of the Au substrate on the MoS_2 energy band structure, a slight improvement of the adsorption energy of the TDMAHf precursor on MoS_2 surface, whereas no major effects on the adsorption energy of H_2O and TMA molecules. This suggests a crucial role of nanoscale morphological effects, such as the experimentally observed local curvature and strain of the MoS_2 membrane, in the enhanced physisorption of the precursors. Afterwards the nucleation and growth of Al_2O_3 and HfO_2 films onto 1L- MoS_2/Au was investigated in details, by monitoring the surface coverage as a function of the number (N) of ALD cycles, with N from 10 to 120. At low N values, HfO_2 exhibits a smaller coverage degree with respect to Al_2O_3 , indicating a slower growth rate of the initially formed nuclei, probably associated to the bulky nature of the TDMAHf precursor as compared to TMA. On the other hand, the formation of continuous films was obtained in both cases for $N > 80$ ALD cycles, corresponding to ~ 3.6 nm Al_2O_3 and ~ 3.1 nm HfO_2 . Current mapping by conductive AFM on these ultra-thin films showed, under the same applied bias, a uniform insulating behavior of Al_2O_3 and the occurrence of few localized breakdown spots in the case of HfO_2 , associated to a less compact films regions. Finally, an increase of the 1L- MoS_2 tensile strain was observed by Raman mapping after encapsulation with both high- κ films, accompanied by a reduction in the PL intensity and spectral shape, consistently with the strain and the higher effective dielectric constant of the surrounding environment. These results demonstrate the highly beneficial role of the Au substrate for the ALD growth of uniform and ultra-thin high- κ dielectrics (Al_2O_3 and HfO_2) on monolayer MoS_2 . An optimized transfer procedure of the high- κ/MoS_2 stack to insulating or semiconducting substrates will be the key for the extensive application of this system in electronics and optoelectronics.

ACKNOWLEDGMENTS

The authors acknowledge S. Di Franco (CNR-IMM) for assistance in the sample preparation and P. Fiorenza and G. Greco (CNR-IMM) for useful discussions.

The paper has been supported, in part, by MUR in the framework of the FlagERA- JTC 2019 project “ETMOS”, by the CNR/HAS bilateral project GHOST-III (2023-25), and by European Union (NextGeneration EU), through the MUR-PNRR project SAMOTHRACE (ECS00000022).

E.S. acknowledges the PON project EleGaN_{Te} (ARS01_01007) for financial support.

B.P and Gy. R. acknowledge funding from the national project TKP2021-NKTA-05.

A.M.M and G. N. acknowledge funding from the European Union’s Horizon 2020 research and innovation programme under grant agreement No 823717 – ESTEEM3.

Part of the experiments was carried out using the facilities of the Italian Infrastructure Beyond Nano.

References

-
- ¹ K. F. Mak, C. Lee, J. Hone, J. Shan, T.F. Heinz, Atomically Thin MoS₂: A New Direct-Gap Semiconductor, *Phys. Rev. Lett.* 105 (2010) 136805.
 - ² A. Splendiani, L. Sun, Y. Zhang, T. Li, J. Kim, C.-Y. Chim, G. Galli, F. Wang, Emerging Photoluminescence in Monolayer MoS₂, *Nano Lett.* 10 (2010) 1271-1275.
 - ³ S. K. Kim, A. Konar, W.-S. Hwang, J. H. Lee, J. Lee, J. Yang, C. Jung, H. Kim, J.-B. Yoo, J.-Y. Choi, Y. W. Jin, S. Y. Lee, D. Jena, W. Choi, K. Kim, High-mobility and low-power thin-film transistors based on multilayer MoS₂ crystals, *Nat. Commun.*, 3 (1011) (2012) 1–7.
 - ⁴ B. Radisavljevic, A. Radenovic, J. Brivio, V. Giacometti, A. Kis, Single-layer MoS₂ transistors, *Nature Nanotech.* 6 (2011) 147-150.
 - ⁵ H. Liu, P. D. Ye, MoS₂ Dual-Gate MOSFET with Atomic-Layer-Deposited Al₂O₃ as Top-Gate Dielectric, *IEEE Electron Device Lett.* 33 (2011) 546–548.
 - ⁶ A. Pakalla, M. Putkonen, in *Handbook of Deposition Technologies for Films and Coatings*, 3rd Ed., (Ed: P. M. Martin), Elsevier, New York **2010**, 364–391.
 - ⁷ H. Liu, K. Xu, X. Zhang, P. D. Ye The integration of high-k dielectric on two-dimensional crystals by atomic layer deposition, *Appl. Phys. Lett.* 100 (2012) 152115.
 - ⁸ T. Park, H. Kim, M. Leem, W. Ahn, S. Choi, J. Kim, J. Uh, K. Kwon, S.-J. Jeong, S. Park, Y. Kim, H. Kim, Atomic layer deposition of Al₂O₃ on MoS₂, WS₂, WSe₂, and h-BN: surface coverage and adsorption energy, *RSC Adv.*, 884–889 (2017) 7.

-
- ⁹ V. K. Sangwan, D. Jariwala, S. A. Filippone, H. J. Karmel, J. E. Johns, J. M. P. Alaboson, T. J. Marks, L. J. Lauhon, M. C. Hersam, Quantitatively Enhanced Reliability and Uniformity of High- κ Dielectrics on Graphene Enabled by Self-Assembled Seeding Layers, *Nano Lett.* 13 (2013) 1162.
- ¹⁰ H. Zhang, G. Arutchelvan, J. Meersschaut, A. Gaur, T. Conard, H. Bender, D. Lin, I. Asselberghs, M. Heyns, I. Radu, W. Vandervorst, A. Delabie, MoS₂ functionalization with a sub-nm Thin SiO₂ layer for atomic layer deposition of high- κ dielectrics, *Chem. Mater.* 29 (2017) , 6772–6780.
- ¹¹ B. Fallahazad, K. Lee, G. Lian, S. Kim, C. M. Corbet, D. A. Ferrer, L. Colombo, E. Tutuc, Scaling of Al₂O₃ Dielectric for Graphene Field-Effect Transistors. *Appl. Phys. Lett.* 100 (2012) 093112.
- ¹² G. Fisichella, E. Schilirò, S. Di Franco, P. Fiorenza, R. Lo Nigro, F. Roccaforte, S. Ravesi, F. Giannazzo, Interface Electrical Properties of Al₂O₃ Thin Films on Graphene Obtained by Atomic Layer Deposition with an in Situ Seedlike Layer, *ACS Applied Materials & Interfaces* 9 (2017) 7761-7771.
- ¹³ T. Park, H. Kim, M. Leem, W. Ahn, S. Choi, J. Kim, J. Uh, K. Kwon, S.-J. Jeong, S. Park, Y. Kim, H. Kim, Atomic layer deposition of Al₂O₃ on MoS₂, WS₂, WSe₂, and h-BN: surface coverage and adsorption energy, *RSC Adv.* 17 (2017) 7 884.
- ¹⁴ A. Iraiwa, D. Matsumura, H. Kawarada, Effect of atomic layer deposition temperature on current conduction in Al₂O₃ films formed using H₂O oxidant, *J. Appl. Phys.* 120, (2016) 084504.
- ¹⁵ L. Cheng, X. Qin, A. T. Lucero, A. Azcatl, J. Huang, R. M. Wallace, K. Cho, J. Kim, Atomic layer deposition of a high- k dielectric on MoS₂ using trimethylaluminum and ozone, *ACS Appl. Mater. Interfaces*, 6 (2014) 11834–11838.
- ¹⁶ J. Yang, S. Kim, W. Choi, S. H. Park, Y. Jung, M.-H. Cho, H. Kim., Improved Growth Behavior of Atomic-Layer-Deposited High- k Dielectrics on Multilayer MoS₂ by Oxygen Plasma Pretreatment *ACS Appl. Mater. Interfaces* 5 (2013) 4739–4744.
- ¹⁷ E. Schilirò, R. Lo Nigro, S. E. Panasci, S. Agnello, M. Cannas, F. M. Gelardi, F. Roccaforte, F. Giannazzo, Direct Atomic Layer Deposition of Ultrathin Aluminum Oxide on Monolayer MoS₂ Exfoliated on Gold: The Role of the Substrate, *Adv. Mater. Interfaces* 8 (2021) 2101117.
- ¹⁸ B. Dlubak, P. R. Kidambi, R. S. Weatherup, S. Hofmann, J. Robertson Substrate-assisted nucleation of ultra-thin dielectric layers on graphene by atomic layer deposition, *Appl. Phys. Lett.* 100 (2012) 173113.
- ¹⁹ A. J. Pollard, E. W. Perkins, N. A. Smith, A. Saywell, G. Goretzki, A. G. Phillips, S. P. Argent, H. Sachdev, F. Müller, S. Hüfner, S. Gsell, M. Fischer, M. Schreck, J. Osterwalder, T. Greber, S. Berner, N. R. Champness, P. H. Beton, Supramolecular Assemblies Formed on an Epitaxial Graphene Superstructure *Angew. Chem.*, 49 (2010) 1794.

-
- ²⁰ H. Zhang, J. Sun, T. Low, L. Zhang, Y. Pan, Q. Liu, J. Mao, H. Zhou, H. Guo, S. Du, F. Guinea, H.-J. Gao, Assembly of iron phthalocyanine and pentacene molecules on a graphene monolayer grown on Ru (0001) *Phys. Rev. B*, 84 (2011) 245436.
- ²¹ E. Schilirò, R. Nigro, F. Roccaforte, I. Deretzis, A. La Magna, A. Armano, S. Agnello, B. Pecz, I. G. Ivanov, R. Yakimova, F. Giannazzo, Seed-Layer-Free Atomic Layer Deposition of Highly Uniform Al₂O₃ Thin Films onto Monolayer Epitaxial Graphene on Silicon Carbide *Adv. Mater. Interfaces* (2019) 1900097.
- ²² E. Schilirò, R. Lo Nigro, S. E. Panasci, F. M. Gelardi, S. Agnello, R. Yakimova, F. Roccaforte, F.; Giannazzo, Aluminum oxide nucleation in the early stages of atomic layer deposition on epitaxial graphene, *Carbon*, 169 (2020) 172-181.
- ²³ S. E. Panasci, E. Schilirò, F. Migliore, M. Cannas, F. M. Gelardi, F. Roccaforte, F. Giannazzo, S. Agnello Substrate impact on the thickness dependence of vibrational and optical properties of large-area MoS₂ produced by gold-assisted exfoliation *Appl. Phys. Lett.* 119 (2021) 093103.
- ²⁴ E. Schilirò, R. Lo Nigro, F. Roccaforte, F. Giannazzo Substrate-Driven Atomic Layer Deposition of High-κ Dielectrics on 2D Materials *Appl. Sci.* 11 (2021) 11052.
- ²⁵ S. McDonnell, B. Brennan, A. Azcatl, N. Lu, H. Dong, C. Buie, J. Kim, C. L. Hinkle, M. J. Kim, R. M. Wallace *ACS Nano*, 7, 11, (2013) 10354–10361.
- ²⁶ K.C. Santosh, R. C. Longo, R. M. Wallace, K. Cho *Computational Study of MoS₂ /HfO₂ Defective Interfaces for Nanometer-Scale Electronics ACS Omega*, 2, 6, (2017) 2827–2834.
- ²⁷ D. Jena, A. Konar, Enhancement of carrier mobility in semiconductor nanostructures by dielectric engineering, *Physical Review Letters* (2007) 98 (13).
- ²⁸ E. Schiliro, P. Fiorenza, G. Greco, F. Monforte, G. G. Condorelli, F. Roccaforte, F. Giannazzo, R. Lo Nigro Early Growth Stages of Aluminum Oxide (Al₂O₃) Insulating Layers by Thermal- and Plasma-Enhanced Atomic Layer Deposition on AlGaN/GaN Heterostructures, *ACS Appl. Electron. Mater.*, 4 (2022) 406–415.
- ²⁹ R. L. Puurunen, Surface chemistry of atomic layer deposition: A case study for the trimethylaluminum/water process, *J. Appl. Phys.* 97 (2005) 121301.
- ³⁰ G. Z. Magda, et al., Exfoliation of large-area transition metal chalcogenide single layers, *Scientific Reports*, 5 (2015) 14714.
- ³¹ S. R. Desai, M. Madhvapathy, D. Amani, M. Kiriya, M. Hettick, Y. Tosun, M. Zhou, J. W. Dubey, D. Ager, A. Chrzan, Javey Gold-Mediated Exfoliation of Ultralarge optoelectronically-Perfect Monolayers, *Advanced Materials*, 28(21) (2016) 4053-4058.
- ³² M. Velický, G. E. Donnelly, W. R. Hendren, S. McFarland, D. Scullion, W. J. I. DeBenedetti, G. C. Correa, Y. Han, A. J. Wain, M. A. Hines, D. A. Muller, K. S. Novoselov, H. D. Abruña, R. M.

Bowman, E. J. G. Santos, F. Huang, Mechanism of Gold- Assisted Exfoliation of Centimeter-Sized Transition-Metal Dichalcogenide Monolayers, *ACS Nano* 12 (2018) 10463–10472.

³³ Y. Huang, et al., Universal mechanical exfoliation of large-area 2D crystals, *Nature Communications* 11 (2020) 2453.

³⁴ M. Velický, et al., Strain and Charge Doping Fingerprints of the Strong Interaction between Monolayer MoS₂ and Gold, *J. Phys. Chem. Lett.* 11 (2020) 6112–6118.

³⁵ E. Pollmann, et al., Large-Area, Two-Dimensional MoS₂ Exfoliated on Gold: Direct Experimental Access to the Metal–Semiconductor Interface, *ACS Omega* 6 (2021) 15929–15939.

³⁶ S. M. Hus, et al., Observation of single-defect memristor in an MoS₂ atomic sheet, *Nature Nanotechnology* 16, (2021) 58–62.

³⁷ M. Cho, H. B. Park, J. Park, S. W. Lee, C. S. Hwang, G. H. Jang, J. Jeong, High-k properties of atomic-layer-deposited HfO₂ films using a nitrogen-containing Hf[N(CH₃)₂]₄ precursor and H₂O oxidant, *J. Appl Phys Lett* (2003) 83:5503.

³⁸ P. Giannozzi, S. Baroni, N. Bonini, M. Calandra, R. Car, C. Cavazzoni, D. Ceresoli, L. C. Guido, M. Cococcioni, I. Dabo, et al. QUANTUM ESPRESSO: a modular and open-source software project for quantum simulations of materials, *J. Phys.: Condens. Matter* 21 (2009) 395502.

³⁹ I. Hamada, Van der Waals density functional made accurate. *Phys. Rev. B*, 89 (2014) 121103.

⁴⁰ H. J. Monkhorst, J. D. Pack, Special points for Brillouin-zone integrations, *Phys. Rev. B*, 13 (1976) 5188.

⁴¹ C. Lee, H. Yan, L. E. Brus, T. F. Heinz, J. Hone, S. Ryu, Anomalous Lattice Vibrations of Single- and Few-Layer MoS₂, *ACS Nano*, 4 (2010) 2695–2700.

⁴² S. E. Panasci, E. Schilirò, G. Greco, M. Cannas, F. M. Gelardi, S. Agnello, F. Roccaforte, F. Giannazzo, Strain, Doping, and Electronic Transport of Large Area Monolayer MoS₂ Exfoliated on Gold and Transferred to an Insulating Substrate, *ACS Appl. Mater. Interfaces*, 13 (26) (2021) 31248–31259.

⁴³ D. Lloyd, X. Liu, J. W. Christopher, L. Cantley, A. Wadehra, B. L. Kim, B. B. Goldberg, A. K. Swan, J. S. Bunch, Band Gap Engineering with Ultralarge Biaxial Strains in Suspended Monolayer MoS₂, *Nano Lett.* 16 (2016) 5836.

⁴⁴ F. Grillo, J. A. Moulijn, M. T. Kreutzer, J. R. Van Ommen, Nanoparticle sintering in atomic layer deposition of supported catalysts: kinetic modeling of the size distribution, *Catal. Today*, 316 (2018) 51-61.

⁴⁵ F. Grillo, H. Van Bui, J. A. Moulijn, M. T. Kreutzer, J. R. van Ommen, Understanding and controlling the aggregative growth of platinum nanoparticles in atomic layer deposition: an avenue to size selection, *J. Phys. Chem. Lett.*, 8 (2017) 975-983.

⁴⁶ J. Pető, G. Dobrik, G. Kukucska, P. Vancsó, A. A. Koós, J. Koltai, P. Nemes-Incze, C. Hwang, L. Tapasztó, Moderate strain induced indirect bandgap and conduction electrons in MoS₂ single layers, *npj 2D Materials and Applications* 3 (2019) 39

⁴⁷ Y. Lin, X. Ling, L. Yu, S. Huang, A. L. Hsu, Y.-H. Lee, J. Kong, M. S. Dresselhaus, T. Palacios, Dielectric Screening of Excitons and Trions in Single-Layer MoS₂, *Nano Lett.* 14 (2014) 5569–5576.